

# Construction and demonstration of a multispectral tomographic scanning imager (TOSCA)

Harald Hovland\*

Norwegian Defence Research Establishment (FFI), Postboks 25, NO-2027 Kjeller, Norway  
\*harald.hovland@ffi.no

**Abstract:** This work presents the first experimental demonstrator of an imager based on a tomographic scanning (TOSCA) principle. The device described generates a stream of multispectral images of a scene or target using simple conical scan optics and a simple patterned reticle, followed by collecting optics and one or several single pixel detectors. Tomographic processing techniques are then applied to the one-dimensional signals to reproduce two-dimensional images. Various aspects of the design and construction are described, and resulting images and movies are shown.

©2013 Optical Society of America

**OCIS codes:** (070.6020) Fourier optics and signal processing; (100.6950) Tomographic image processing; (110.0110) Imaging systems; (110.3010) Image reconstruction techniques; (110.4234) Multispectral and hyperspectral imaging; (110.6960) Tomography.

---

## References and links

1. H. Hovland, "Tomographic scanning imager," *Opt. Express* **17**(14), 11371–11387 (2009).
2. H. Hovland, "Specialized tomographic scanning imaging seeker," *Proc. SPIE* **5778**, 725–731 (2005).
3. A. C. Kak and M. Slaney, *Principles of Computerized Tomographic Imaging* (IEEE Press, 1988).  
<http://www.slaney.org/pct/pct-toc.html>.
4. P. C. D. Hobbs, *Building Electro-Optical Systems* (John Wiley & Sons, 2000).
5. P. Mouroulis, R. O. Green, and T. G. Chrien, "Design of pushbroom imaging spectrometers for optimum recovery of spectroscopic and spatial information," *Appl. Opt.* **39**(13), 2210–2220 (2000).
6. R. D. Hudson, *Infrared System Engineering* (John Wiley & Sons, 2006).
7. J. Hsieh, *Computed Tomography Principles, Design, Artefacts, and Recent Advances* (SPIE Optical Engineering Press, 2003).
8. E. Hecht, *Optics* (Addison-Wesley, 2001).
9. J. S. Accetta and D. L. Shumaker, *The Infrared and Electro-optical Systems Handbook*, Vol. 1 (Infrared Information Analysis Centre, 1993).
10. Thorlabs web pages, <http://www.thorlabs.com>.
11. Hamamatsu web pages, <http://www.hamamatsu.com>.
12. W. H. Press, "Discrete Radon transform has an exact, fast inverse and generalizes to operations other than sums along lines," *Proc. Natl. Acad. Sci. U.S.A.* **103**(51), 19249–19254 (2006).
13. E. J. Candès, J. Romberg, and T. Tao, "Robust uncertainty principles: exact signal reconstruction from highly incomplete frequency information," *IEEE Trans. Inf. Theory* **52**(2), 489–509 (2006).

---

## 1. Introduction

Tomographic scanning (TOSCA) imaging was presented earlier [1] as an alternative way of acquiring images using various types of radiation. It was shown that a single pixel sensor combined with a simple circular scan mechanism could produce images with better signal-to-noise ratio than achievable with classical single pixel imagers using 2-dimensional scanning.

Here, the first experimental demonstration of a working camera based on the TOSCA principle is reported. The aim of this TOSCA demonstrator is to show a practical implementation of the TOSCA imaging principle, together with artefacts that can be associated with such a system. The camera design is presented, including the signal processing necessary for the image reconstruction. Sources of noise and systematic errors are discussed. Simulations highlight important design considerations. Experimental results demonstrate that a single-pixel imager using a Si avalanche photodetector can generate useful

images well above the noise floor under moderately bright and strongly varying light conditions.

## 2. TOSCA design

### 2.1 Basic principle

The basic TOSCA sensor is illustrated in Fig. 1(a). Here, thin line detectors are scanned across the scene at regularly distributed detector orientation angles, each scan producing 1-dimensional projection of the scene. The reconstruction process, described in detail in [1] and summarized in section 5.3, is similar to that used in parallel beam X-ray CAT scanners.

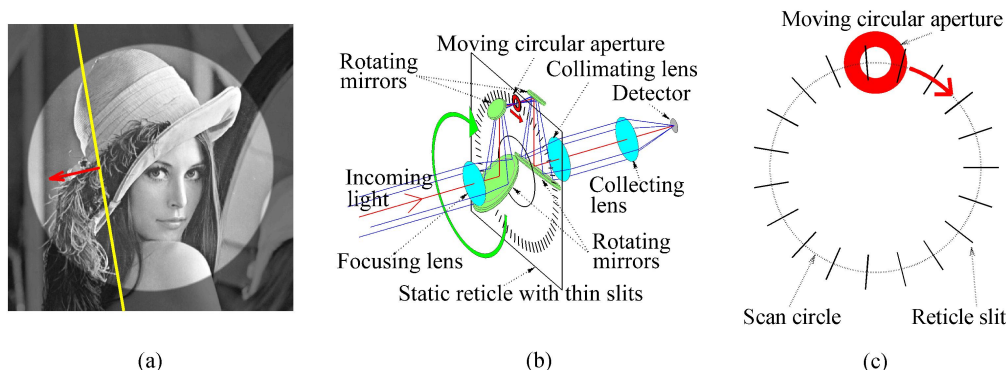


Fig. 1. (a) Schematic image of a line scan: A thin line detector (yellow line) scans across the image of the scene. (b) Realization chosen in this work. The mirrors (green) and the moving circular aperture (red) rotate together as a unit around the optical axis of the incoming light. The use of a mirror pair to decenter the image on the reticle keeps the image orientation fixed relative to the reticle, making the thin slits scan the image at regular angular intervals. (c) Reticle pattern and moving aperture layout. The interior of the aperture (in red) defines the field of view, moving in a circular pattern indicated by the dashed circle. The use of an aperture enables the use of a single detector element to make all the angular scans.

The TOSCA principle can be realized in several ways. Using a circular array of line detectors is advantageous in terms of noise, size and bandwidth [2]. In the single pixel configuration, the optics could be kept stationary while the reticle is moved. Several solutions with circular translational and rotational movements were examined, but all had issues with complexity, bulkiness or other, and none are pursued further here.

The configuration chosen for this work is shown in Fig. 1(b) and 1(c). Basically, the system consists of focusing optics to image the scene, two pairs of mirrors acting as rotating periscopes to move the optical axis sideways, through a reticle, and back to the rotational axis, where lenses collimate, then collect the light onto a detector. The image is scanned sequentially by thin transparent slits on the static reticle, oriented at regularly distributed angular intervals. A circular aperture rotating with the periscopes serves as a field stop.

Restricting the field of view (FOV) in a TOSCA system removes the effect of finite reticle slit or line detector length [2]. If a single detector is used to perform different angular scans the aperture also separates signals from different angular scans. Circular apertures can be rotated without affecting the FOV, possibly simplifying the design.

The focusing optics requirement is somewhat relaxed compared to conventional optics: Image sharpness is only critical in the scan direction. In the direction along the slit, the signal is integrated across the FOV. The design target is thus to create a narrow line width across the reticle slit or detector line, rather than to create a small spot size.

The detector thus generates a signal corresponding to a sequence of line scans at regularly distributed scan angles. The line scan signal sequence is then amplified, digitized and processed using tomographic reconstruction algorithms to produce an image of the scene.

## 2.2 Optics, optoelectronics and A/D conversion

The system main optomechanical components consist of the following:

1. Focusing optics, consisting of a 25.4 mm diameter, 75 mm focal length (FL) lens.
2. First rotating periscope, consisting of a 35.4 mm × 25.0 mm elliptical enhanced aluminum coated flat mirror, and a 12.7 mm diameter protected silver flat mirror.
3. Circular field stop. This 4.0 mm diameter circular aperture is made out of 0.2 mm thick Nickel/Teflon coated stainless steel.
4. The reticle is a metal coated 2.3 mm thick glass substrate (photolithography master mask) with 65 thin line segments each 6.0 mm long and 70 μm in a circular pattern. The distance from the center to each slit center is 43.0 mm. An odd number of slits avoids redundant information from parallel line pairs [1].
5. Second periscope, similar to the first, to realign the optical and rotational axis.
6. Collimating/collecting optics, consisting of a 30 mm diameter, 80 mm FL lens, and a 25.0 mm diameter, 20 mm FL aspheric lens.
7. Detector. The unit chosen was a Hamamatsu C5460-01 Si avalanche photodetector module, with a 3 mm diameter active area, and a 100 kHz detector bandwidth.

The camera was designed to use low-cost off-the-shelf optical components wherever possible. The optics was designed to handle wavelengths within the 400-1700 nm range, where relatively inexpensive optics and (uncooled) detectors with decent performance are available. A focal plane line width was chosen to be 70 μm, determined more by moving parts in the scanning system (due to the roller bearings) than the optical limits. It was decided that a minimum 64 pixels across the reconstructed image would be sufficient for a useful general purpose image. Slaney and Kak [3] reported an equal number of angular scans and samples/scan to be suitable for general purpose imaging, and it was decided that 65 angular line scans with at least 65 samples/scan would be suitable, giving 4225 samples/frame. The 100 kHz bandwidth available with some large detectors enables ~25 Hz video rate imaging.

Combining the periscope scan mechanism with a single pixel detector means the scan circle radius is large compared to the FOV diameter on the reticle [1]. The FL of the focusing optics must equal or be larger than the sum of the scan circle radius and the optical entrance aperture diameter, as Fig. 1(b) indicates. A small setup was favored given the high rotational rate, and the approximate 4.5 mm FOV diameter on the reticle given by the line width and the initial number of lines in a scan was found suitable for 1" diameter optics.

Through simulations, a solution was found with a 43 mm scan circle radius, 1" diameter and 75 mm FL focusing optics, giving a 4.16 mm distance between scan lines. Aliasing is then avoided with a 4.0 mm aperture, giving a 53 mrad (~3°) full angle FOV. ZEMAX simulations showed the spot size would be smaller than the slit width within a 0.8 mm focusing zone. After the reticle the light is brought back to the rotational axis using a periscope. The reticle metallization side faces the incoming beam to limit stray light.

After an 80 mm FL lens, the collimated optical beam could be split in several spectral channels using beam splitters, and then focused onto separate non-imaging detectors using lenses. The detector size is minimized to limit noise. Optimization through ZEMAX simulations showed a 20 mm FL aspheric lens to be an efficient solution. Assuming spectrally homogeneous incoming light within the 400-1700 nm range, 99% of the light would hit the detector within a 1.35 mm diameter circle.

Even with a low-noise large-area PN detector, high capacitance (typically hundreds of pF) make them incompatible with the high bandwidth requirements (~100 kHz), even using cascode amplifiers [4] with state-of-the-art operational amplifiers. Avalanche or PIN photodiodes are a better choice, due to lower capacitance (a few pF). The Hamamatsu C5460-01 avalanche photodetector module was chosen due to bandwidth, low noise, and a fully characterized amplifier design with a suitable gain, reducing risk and development time.

The analogue to digital conversion prior to digital signal processing and display was done using a National Instruments NI PCI-6123 16-bit, 500 kS/s/ch simultaneously sampling card.

The sample rate can easily be modified in this setup, but we will in the following assume 119 samples/scan, higher than the originally 65 indicated. This makes the sample scan step versus slit width ratio near integer. An integer ratio means the resulting signal intensity due to a point source will be independent of its position. The oversampling can reduce quantization and aliasing errors, if the resulting signal is appropriately filtered.

### 3. Experimental set-up

Compared to the system described in section 2.2, the sampling rate of the A/D card was set to 200 kHz for each channel, with subsequent resampling as described in the following. The frame rate was  $\sim 25$  Hz in all experiments.

The rotating optical unit base is a single piece of machined aluminum mounted with roller bearings, as seen in Fig. 2(a). The mirrors forming the two periscopes are first surface mirrors, mounted with the reflecting surfaces towards the aluminum unit for better tolerances. The focusing and collimating optics are mounted in sideways adjustable holders using nylon-tipped set screws, and longitudinally adjusted with shims. The circular aperture was aligned with, and glued to the rotating unit using a jig, the soft coating facing the reticle.

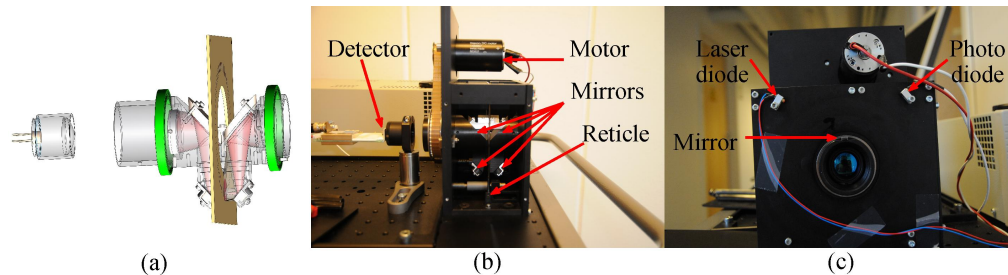


Fig. 2. (a) Semi-transparent view of the rotating optics, reticle and detector unit. (b) Experimental TOSCA setup. The motor (top) drives the scan unit (centre) using a belt drive. The lens/ detector/amplifier assembly (left) is mounted on a post holder. The scan head and detector was enclosed to avoid stray light. (c) Laser based tachometer. A laser (top left, connected by red/ blue leads) was pointed at a mirror, mounted on top of the rotating unit. At each turn, the reflected light hit a photodiode, creating a sharp flank pulse used as an absolute angular reference.

Optics alignment was achieved by adjusting the focusing lens to minimize the aperture border circular movement as seen from several meters in front of the optics, the aperture back illuminated without the reticle. The reticle was first mounted in a plane between three adjustment screws with opposing springs, and was then aligned sideways by looking from the collimator side, where the slits should bypass the aperture by equal amounts in all orientations. The collimating optics was aligned with a bright light source several meters in front of the rotating optics (with the reticle mounted), adjusting the collimating lens sideways until the source appeared stable, as seen through the collimator.

Counterweights were used to minimize vibrations due to first and second order moments. The rotating unit was driven via a belt drive by a DC motor, as shown in Fig. 2(b). The motor was powered by a 13.7 V, 7.0 A regulated power supply.

A 5 mm square mirror was fixed to the side of one of the ends of the rotating unit, facing outwards. Light from a collimated laser source hitting the mirror when the latter faced upwards was collected by a simple photodiode with integrated collector optics, as shown in Fig. 2(c). The rising flank of the electrical pulse at each revolution was used as an absolute position trigger. Recording this gave a relative jitter of  $\pm 0.25\%$  of the roundtrip time.

This jitter level makes it necessary to resample the detected signal, as simulations (section 5.5) show that the image starts to deteriorate even with single sample shifts, making the trigger mechanism unsuitable as a sole reference. If the detector signal is significant at all time, the trigger can still be combined with the detector signal to get a useful reference:

The camera is sealed to avoid stray light. Without overlap between the rotating aperture and the reticle slits, little light reaches the detector. As the aperture starts to sweep across a slit, the signal starts increasing. The signal normally increases, and then decreases until the aperture and slit no longer overlap, as shown in Fig. 3(a). Noise can make it difficult to determine the exact minimum signal position. A running (cosine segment) smoothing filter suppressed the signal noise fairly well, enabling position location. The minima sample positions were smoothed out to reduce time step quantisation errors. These sample minima correspond to regularly distributed angular orientations of the rotating unit. The signal was then resampled using linear interpolation to get estimated constant angle step sample points. The laser pulse position then determined absolute angular orientation.

With a relatively tight drive belt, a multi-component oscillation was observed in the minimum signal time intervals. The biggest components corresponded to the motor rotation frequency and the optical unit rotation frequency, likely caused by cogwheel eccentricity and tilted roller bearings/fixtures. Loosening the belt reduced oscillations, removing motor cogwheel contributions. Figure 3(b) shows the resulting frequency components.

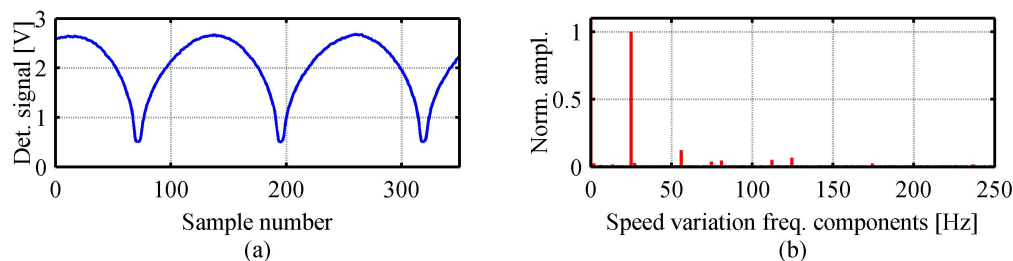


Fig. 3. (a) Signal recorded from the Hamamatsu detector module (inverted). Minimum signal occurs when reticle slit and aperture do not overlap. (b) Rotation frequency components, measured by intervals between detector signal minima. The 25 Hz peak is the optics spin frequency.

## 4. Experimental imaging results

### 4.1 Single point reconstruction

Single point sources, homogeneous and complex scenes were used to characterize the system. Recordings of single points were made at several FOV locations, using a 2 mm diameter spot from a 1.3 mW, 543 nm HeNe-laser reflecting off white paper, located 5.12 m from the camera. The spot featured some visible speckle. The paper was illuminated by an opposing white wall illuminated by sunshine through windows. An illumination level of  $320 \text{ lux} \pm 5\%$  was measured using a lux meter in front of the paper, indicating the background was fairly homogeneous, and much dimmer than the reflected laser spot. The paper was estimated to diffusely reflect  $\sim 90\%$  of the incoming light, filling the FOV. By estimating the TOSCA camera spectral responsivity bandwidth to be  $\sim 4$  times larger than that of the luxmeter, and that the reflected sunlight is relatively constant over the detector spectral range, rough calculations indicates that the radiant power from the reflected laser spot should be  $\sim 1\%$  the radiant power of the remaining reflected light from the whole 30 cm diameter circular disc seen by the camera. The 0.9% value determined from Fig. 4(a) is in good agreement with this estimate. The laser spot was moved to produce different single point reconstructions.

Reconstructions of centered and de-centered spots are shown in Fig. 4(b) and 4(c). In both cases, the reconstructions exhibit a peak centered at the laser spot, surrounded by a ring of slight unstructured “noise”, then a ring with radial modulation, a region with slightly less structured modulation pattern, and then again a new modulation pattern, resembling the results obtained in simulations (section 5.3), except that the simulated main lobes are thicker.

Temporal noise figures were determined by illuminating the paper as before, but with higher intensity. Lux measurements now gave reading of  $2000 \text{ lux} \pm 10\%$ . We now assume the spectral distribution to be similar to that measured during the point reconstructions.

Measurements with the laser spot, gave ratios consistent with previous measurements. Temporal statistics of each pixel in a 101 frame recorded reconstruction of the homogeneous background were made. The temporal mean and standard deviation values, a histogram of values within the field stop are shown in Fig. 5(a), 5(b) and 5(c). The noise is strong at the aperture border. We now focus on the region inside the border. Figure 5(d) shows the relative noise level as a function of distance (in pixel units) from the image center. The noise level error bars shorten with eccentricity due to the higher number of pixels considered.

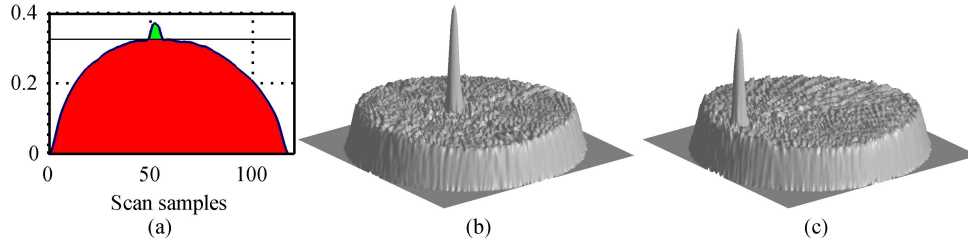


Fig. 4. (a) Laser spot (green) and background illumination (red) contributions in a measured scan signal. The ratio of these areas is 0.009, close to the predicted 1%. Reconstruction of (b) centered and (c) de-centered laser spot reflected off a homogeneous background.

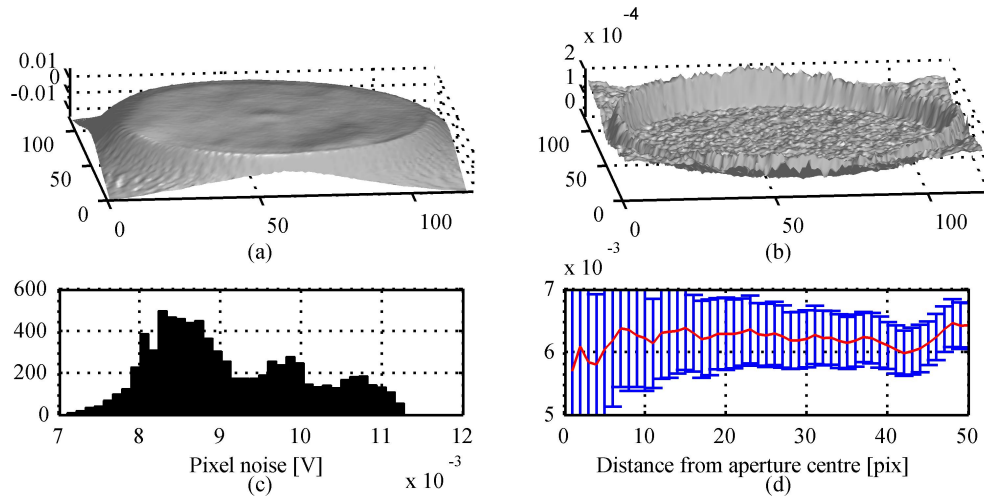


Fig. 5. Temporal statistics of 101 subsequent reconstructed frames: (a) Mean value. (b) Temporal standard deviation. (c) Histogram. Only pixels within a 50 pixel radius are accounted for to minimize the effect of the field stop. (d) Relative noise level (red curve) as a function of distance to the reconstructed image center, in reconstruction pixel units.

To assess the photoelectron number generated per frame, we start by estimating the number of photons arriving at the camera entrance aperture. The reflection of the 1.3 mW, 543 nm HeNe laser corresponded to 0.9% of the reflected output when the copying paper source was illuminated with 320 lux light. With a diffuse reflectance of 0.9, the 2000 lux figure is equivalent to 0.81 W diffusely radiated at 543 nm. Including the optics transmission of 0.7, the 22 mm entrance aperture optics at a 5.12 m distance captures an equivalent 2.6  $\mu$ W from the scene. The FOV pixels are exposed for 10  $\mu$ s per angular scan. 65 scans per frame gives a 0.65 ms total exposure time per frame, with a total of 1.8 nJ arriving on the detector. These are distributed onto the  $10.5 \times 10^3$  pixels within the FOV. The detector responsivity at 543 nm being 0.2 A/W (without the avalanche gain), each pixel receives  $1.34 \times 10^{-13}$  C, or  $2.1 \times 10^5$  photoelectrons per pixel, resulting in  $4.6 \times 10^2$  center pixel photon noise. This noise is incoherently added to the  $1.2 \times 10^3$  photoelectrons of detector noise calculated in section 5.2, giving a total noise of  $1.3 \times 10^3$  photoelectrons. The resulting relative noise level then

becomes  $6.2 \times 10^{-3}$ , in good agreement with Fig. 5(d). The theory presented in section 5.2 indicates a 20% reduction in photon noise at the border relative to the center noise. The relative rim noise level would then be  $6.0 \times 10^{-3}$  if the FOV border effect is ignored. This is consistent with the trend of Fig. 5(d), but the results are inconclusive, given the data uncertainty.

#### 4.2 Mono- and multispectral TOSCA imaging

An image from the first single channel TOSCA video ([Media 1](#)) is shown in Fig. 6(a). This was recorded using the same illumination conditions as in section 4.1.

To demonstrate multispectral operation, a Thorlabs FD2G green interference filter was used as a 45° spectral beam-splitter after the collimator lens. The two resulting light beams were then collected using two lens/detector pairs. The modified setup is shown in Fig. 6(b).

Operation was similar to before. The images from the 'non-green' and 'green' channels are shown in Fig. 6(c) and 6(d), respectively, and a merged two-channel image is shown in Fig. 6(e). In this image, the black/white pattern is of particular interest. Both 'non-green' and 'green' dominance is visible elsewhere, but does not appear in any black/white transition. Color artefacts can often be visible at such transitions in traditional multispectral cameras with spectral misalignment, and can cause problems when looking for objects with a specific spectral signature, particularly when looking at sub-pixel targets on a homogeneous background [5]. In the TOSCA camera this problem is different, as the image geometry is defined by the narrow reticle slits and the aperture, which are common for all spectral components. Similar artefacts might instead appear if characteristics of the detector/amplifier chains of different spectral channels differ. Artefacts due to the point spread function could also affect this issue, as the color of a strong intensity peak would create surrounding ripples.

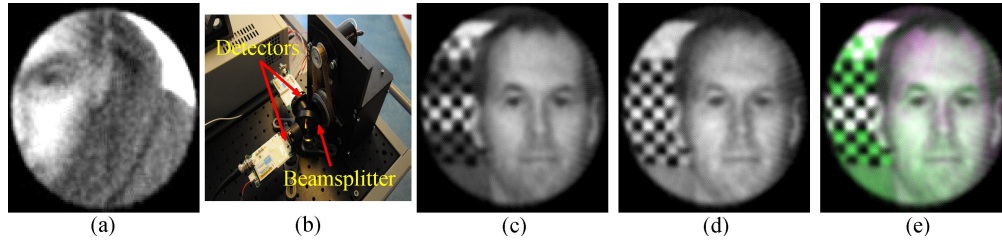


Fig. 6. (a) Frame from the first single channel TOSCA movie ([Media 1](#)) recorded using the experimental system. (b) Multispectral TOSCA setup. A spectral interference filter splits the beam in two. Each beam is detected with a lens/detector pair. (b)-(d) Author image with green/white, green/ black and white/black checkerboard patterns in (b) 'non-green' channel, (c) 'green' channel and (d) a color-coded combined image. The white/black checkerboard pattern transition color purity is due to perfect alignment between channels, inherent in the TOSCA system.

## 5. Design considerations

### 5.1 Sources of noise and systematic error

In a TOSCA system, artefacts can occur in the image if the scene is undersampled [3], and an application-dependent tradeoff can be made between the image quality and the requirements on the camera hardware. To completely avoid aliasing, the Nyquist criterion must be met at the aperture periphery. The highest spatial frequency  $k_{max}$  supported due to angular scan limitations is given by the number of angular scans  $N$  and the aperture diameter  $D$ :

$$k_{max} > N/(\pi D) \quad (1)$$

In the worst-case, the system presented here supports spatial frequencies corresponding to ~20 line pairs across the aperture diameter due to the limited number of angular scans. If the region of interest is a small structure on a homogeneous background, the spatial frequencies

supported will be higher, typically limited to the sampling density, and as a bonus, the artefacts are separated from the target.

Photon noise arises due to arrival statistics. The TOSCA measurement principle leads to a spatial smoothing of this noise [1].

Errors are induced by the scanning, for example due to rapidly moving or varying objects. Optical and optomechanical errors and noise sources due to imperfections and limitations in the optics and the scan mechanism also limit the system performance. The lack of angular resolution was covered in [1], and the general problem of undersampling in tomographic reconstruction is treated in [6]. Other errors arise due to detector response imperfections such as non-linearity, non-homogeneous frequency response and calibration errors, analogue signal conditioning and the digital-to-analogue conversion process, together with noise arising from the corresponding components. The TOSCA measurement principle also smoothes out detector noise spatially [1]. Finally, imperfections in the digital filtering and reconstruction methods can also contribute to image degradation.

Many of these effects are well described in textbooks [6–9]. We will here focus on those specific to the TOSCA configurations, namely geometrical and timing errors. Some of these errors are also explained further and exemplified through simulations in section 5.5.

With a misaligned circular aperture, the FOV moves in a small circle in the scene, and only parts of the angular spectrum of the peripheral structures are reproduced, leading to essentially peripheral artefacts. The misalignment is characterized by a revolving vector.

Reticle slits may be misaligned laterally or angularly. A translational reticle slit dislocation represents approximately a co-ordinate system shift. Unless two reticle slits are visible jointly through the circular aperture, the equivalent of a time shift can compensate such errors; using a sufficiently small aperture will avoid such double exposure. An overall rotational error implies an equal offset error for all lines, plus a common rotational error as the sampling and reconstruction lines are misaligned. Line scan signals due to a point will be shifted by a specific distance. The point spread function then becomes a circle, turning points into circles, and lines into line pairs. Edge artefacts will also occur. This rotational error is similar to an overall timing error, with the exception of the overall rotation.

## 5.2 Photon budget

Prior to construction, a theoretical analysis was made using real component data to see if the system can produce signals beyond noise. The reference target is a 25% reflectance horizontal Lambertian gray body, illuminated by the sun in zenith through a 1976 U.S. standard atmosphere. Figure 7(a) shows the resulting target spectral radiant exitance  $M_\lambda$  from published LOWTRAN 7 data [9]. A short scene-camera-distance is assumed, and the resulting atmospheric effects are ignored. Internal optics transmission/reflection losses are accounted for.

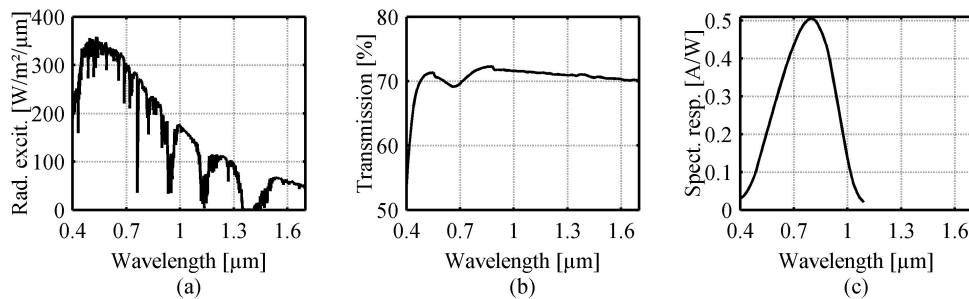


Fig. 7. (a) Spectral radiant exitance from a 25% diffusely reflecting, horizontal test target in the 1976 U.S. standard atmosphere [9] with an air mass index  $m_a = 1.0$ , the sun being in zenith. (b) Optics transmission for light passing through the reticle slit in the proposed system. (c) Spectral responsivity of the Hamamatsu C5460-01 detector, not including the avalanche gain.

The optics consists of 3 lenses, 4 mirrors and one reticle. With BK-7N surface transmission data and protected silver coating mirror reflectance data found on Thorlabs' web sites [10], a ~70% transmission is found in Fig. 7(b). The Hamamatsu C5460-01 detector spectral responsivity [11] is shown in Fig. 7(c). Diffraction losses are being ignored as the reticle slit width is much larger than the wavelength. Besides the ~30% optical loss, all light passing through the entrance aperture, the rotating aperture and the reticle are assumed to hit the detector. Consider an image pixel as a 70  $\mu\text{m}$  side square in the reticle plane. With the 75 mm FL, the image pixel solid angle is  $\Omega_{px} = 8,7 \times 10^{-7}$  sr. A Lambertian target filling the pixel illuminates the entrance aperture with spectral intensity:

$$P_{Px,\lambda} = M_\lambda A_{Ap} \Omega_{Px} / \pi \quad (2)$$

With a 25 Hz frame rate, 65 slits and 119 samples/scan, the sample interval is  $\Delta t = 5.1 \mu\text{s}$ . The number of photoelectrons  $\langle S_{e,sample} \rangle$  generated by light incident on a pixel-size area of the reticle slit is:

$$\langle S_{e,sample} \rangle = e^{-1} \Delta t \int P_{Px,\lambda} R_\lambda \tau_\lambda d\lambda = (\pi e)^{-1} \Delta t A_{Ap} \Omega_{Px} \int M_\lambda R_\lambda \tau_\lambda d\lambda = 9.4 \times 10^4, \quad (3)$$

with the electron charge  $e$ , the detector spectral responsivity  $R_\lambda$  and the optical spectral transmission  $\tau_\lambda$ . The total number of photoelectrons per image pixel is the sum from each angular scan:

$$\langle S_{e,frame} \rangle = N \langle S_{e,sample} \rangle = 6.2 \times 10^6 \quad (4)$$

To determine the actual "photon noise" of the photoelectron signal, some assumptions must be made. Only the FOV contributes to the photon noise. The detector sees an entire line within the circular aperture, meaning "hot spots" can give significant noise contributions to low intensity areas. Even homogeneous scenes produce uneven spatial noise distributions: Central pixels get more noise since the average line segment size, defined by the slit and the circular aperture, decreases away from the center (where the line length is the full diameter for all angles). The center noise level is ~1.25 times that at the rim, with an asymptotic value of  $(\pi/2)^{1/2}$  in the limit of narrow scan lines relative to the FOV diameter. If the reference target fills the FOV, the center pixel photon noise level  $\langle N_{p,frame} \rangle$ , given as the square root of the total number of photoelectrons collected in the central pixel, is therefore a conservative estimate:

$$\langle N_{p,frame} \rangle = \sqrt{\langle S_{e,frame} \rangle} = 2.5 \times 10^3 \quad (5)$$

The Hamamatsu C5460-01 noise equivalent power (NEP) is  $2 \times 10^{-14}$  W/ $\sqrt{\text{Hz}}$ , at the peak responsivity  $R_{Max} = 0.5$  A/W. The detector sample noise level  $N_{d,sample}$  in photoelectrons is:

$$N_{d,sample} = \frac{R_{Max} NEP \sqrt{\Delta t}}{e} = 1.4 \times 10^2 \quad (6)$$

The detector noise can be expressed as an equivalent number of frame pixel photoelectrons by incoherent addition of the 65 angular scans:

$$\langle N_{d,frame} \rangle = \sqrt{N} \langle N_{d,sample} \rangle = 1.2 \times 10^3 \quad (7)$$

This is about half of the photon noise and leads to a degradation of the signal-to-noise ratio by about 12%, compared to photon noise alone. The chosen example is thus close to the detector noise floor. However, as can be seen in the simulations in section 5.6, spatial averaging makes image features visible at even lower signal levels.

Using the initial reference target and introducing beam splitters and multiple detectors, the detector noise per channel is unchanged. The signal is split between the detectors, and the photon noise per channel is therefore reduced. If the signal is equally split in 4 channels, the

photon noise per channel is halved, equaling the detector module noise. The signal-to-noise ratio is then  $9.1 \times 10^2$ . Exploiting the range beyond the Si spectral band using InGaAs detectors do not affect the Si detector performance, but such detectors are typically noisier.

At the given light levels, the sensor is still photon noise limited, but for lower light levels the detector noise becomes the dominant source, and the signal to noise ratios then scales with the signal level. If the reference target is observed during overcast weather, the light level could be reduced by some 2 orders of magnitude, making detector noise significant.

### 5.3 TOSCA simulation tool

A simulation tool was developed in MATLAB to aid the design of an experimental realization. The software is available from the author upon request. The tool consists of:

- Scene generation. An arbitrary image is used as input, and photon shot noise is simulated.
- Circular aperture generation and superposition on the image. Parameters specify the aperture/scene misalignment, inducing a circular aperture movement relative to the scene.
- Reticle generation. Specifies the physical reticle shape, including overall offset and misalignment, as well as shape, position and orientation errors of each individual slit.
- Scan movement generation. Includes rotational errors and individual sample errors.
- Detection process, including detector/electronics noise generation and timing jitter.
- Reconstruction process using filtered back projection.

The filtered back projection is described in detail in [1]. Briefly, the steps are as follows:

- Each angular scan is zero-padded and FFT'ed to replace the discrete Fourier transform.
- The FFT components are multiplied element by element with a modified ramp filter to enhance high frequency components. This filter multiplies the frequency components by a coefficient proportional to the absolute value of the corresponding frequencies, except the DC coefficient value, set to  $\frac{1}{4}$  the value of the lowest non-zero frequency coefficient.
- The filtered signal is inverse FFT'ed, giving the filtered back projection function.
- A matrix is filled with interpolated values of the filtered back projection function using the pixel positions orthogonally projected onto the scan line as input.
- The angular scan matrices are added together to complete the reconstruction

In the following, we separate between the image pixels in the reticle focal plane and the reconstruction (matrix) pixels; these can differ in size. The input image used in simulations has a much higher resolution than the simulated camera.

### 5.4 Simulated reconstruction accuracy

The reconstruction technique used here is not unique, but is useful for real-time imaging, being fast and yielding relatively high resolution. It can, however, produce artefacts surrounding positive or negative spikes, especially with limited angular resolution. Alternative approaches, such as using an iterative search, could provide a better image reconstruction [3,12,13], but such algorithms are often application-specific and computationally demanding.

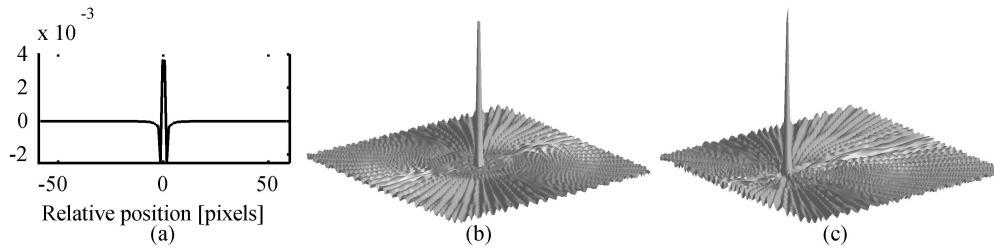


Fig. 8. (a) Filtered back projection function and (b) reconstruction of a  $512 \times 512$  image with a single centred unit pixel. (c) Reconstruction of a  $512 \times 512$  image with a de-centred unit pixel.

Figure 8(a) shows a single scan filtered back projection of a  $512 \times 512$  pixel image with a single centered spike. The dips on both sides of the peak compensate line features from scans in other directions. Figure 8(b) shows a mesh plot of a centered and 8(c) a de-centered single pixel image reconstruction. Both reconstructions contain a central peaked main lobe, a transition region with irregular modulation, and then radial ripples, splitting in two due to the slit width. All modulations outside the main lobe are within  $\pm 5\%$  of the peak value.

A sample reconstruction without noise or misalignment was made with a  $512 \times 512$  pixel image 'Lena', shown in Fig. 9(a). Figure 9(b) shows the reconstructed image using a  $118 \times 118$  pixel grid. Reconstructing onto a  $512 \times 512$  pixel grid removes the effect of the pixel borders, as seen in Fig. 9(c). Line artefacts appear due to a combination of low angular and high spatial resolution, seen in the prolongation of the hair line structure across the brim of the hat.

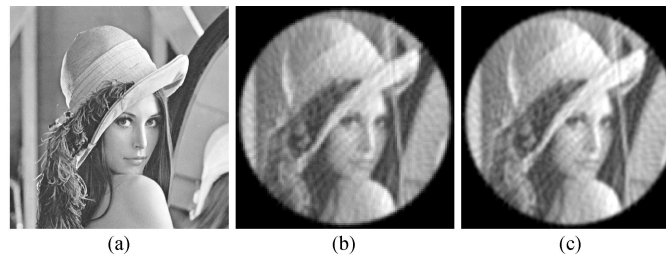


Fig. 9. (a) Original  $512 \times 512$  pixels high resolution 'Lena' image. Reconstruction using a 65 slit reticle, with 119 samples/scan, onto a  $118 \times 118$  (b) and  $512 \times 512$  (c) pixel grid.

### 5.5 Geometrical and timing errors

If the aperture is misaligned with the optical axis, as described in Fig. 10(a), the aperture has a circular movement with respect to the nominal FOV, characterized by its radius and phase relative to the optics rotation. Resulting artefact are shown in Fig. 10(b), 10(c) and 10(d), with a misalignment radius corresponding to 10% of the aperture diameter and a misalignment phase of  $0^\circ$ ,  $45^\circ$  and  $90^\circ$ , corresponding to an aperture shift parallel, oblique and normal to the reticle lines, respectively. Compared with Fig. 9(b), the shift normal to the reticle lines create a dark ring around the scene and a light background outside the aperture, whereas the shift parallel to the lines blurs rim features more subtly, as angular components are fetched from other parts of the image with similar intensities. This is more easily seen in gradient images.

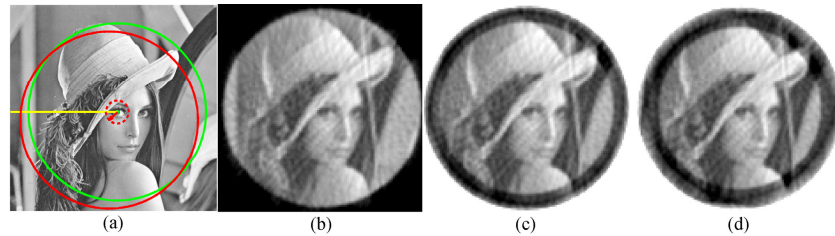


Fig. 10. Aperture misalignment: (a) Misaligned (red) aperture is displaced from its ideal location (green). A red vector indicates eccentricity relative to the direction towards the rotational axis (yellow). The misalignment rotates (dashed red circle), the aperture hiding different scene parts during the scan. (b-d): Reconstructions with aperture misalignments corresponding to 10% of the aperture diameter, with the phase angle being  $0^\circ$  (b),  $45^\circ$  (c), and  $90^\circ$  (d).

The distortion arising from a reticle rotation or a time shift is due to a change in the point spread function from a spike to a circle, as illustrated in Fig. 11(a). The effect is shown with time shifts corresponding in Fig. 11(b) to 1, Fig. 11(c) to 5 and Fig. 11(d) to 40 samples (recalling that a single scan takes 119 samples). A 1 sample time shift already gives a visible effect: The eyes are smeared out, and the hat brim has a surrounding halo. With a 5 sample time shift a ‘double view’ effect appears, with lines split in two. Also, an outer dark ring resembling that found in Fig. 10(c) appears. A 40 sample time shift distorts the scene totally. Varying the time delay, a characteristic dark halo surrounding the circular image appears at significant time shifts, and when the time shift is reduced, the double line features are found to approach each other. Due to this effect, precise means for measuring scan orientation are necessary.

Using a trigger signal produced once per rotation can correct the previous effect, and enable long term orientation stability, but scan errors can still be introduced by a varying scan speed. We now focus on the effect of shifts caused by speed variations between two triggers. Noting that the distance between two consecutive triggers represents exactly one revolution, we can use resampling to force a zero phase error at these reference points. The phase error in the sample points can then be modeled as a sum of sine waves in between. Figure 12(b) shows the effect of a phase shift in the range  $\pm 5$  samples, varying sinusoidally with the rotation. The overall image resembles a shifted version of the ideal reconstruction in Fig. 9(b), with an artefact in the region outside the aperture. With a speed variation frequency twice the rotational speed, the effect is visually more dramatic, as seen in Fig. 12(c), resembling that of the constant time shift error in Fig. 11(c). Simulations show higher speed variation frequency components also give important distortions. The triggered system can thus handle variations with frequencies lower than the rotational speed, but higher frequency variations can clearly cause problems. Potential sources of problems are roller bearings for the rotating optical assembly, the motor as well as its power supply, and the transmission linking the rotating unit and the motor. High rotational inertia reduces this effect.

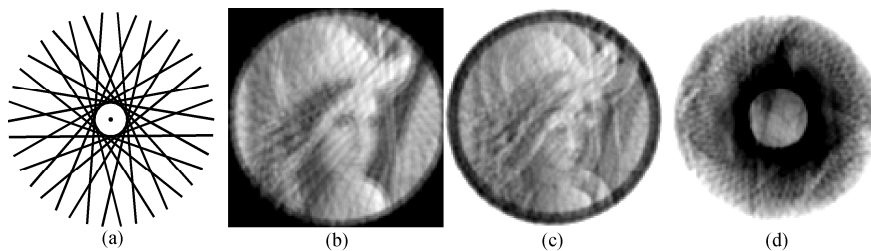


Fig. 11. Line shift errors: Effect of a constant difference between assumed and real scan line location. (a) The footprint of scan lines at the time where the reconstruction assumes them to pass through the center. This causes point spread function to essentially become a circle-like structure. This error can be due to a fixed timing error or an angularly misaligned (rotated) reticle. Reconstruction similar to that in Fig. 9(b), but with time shift errors, corresponding to (b) 1 sample, (c) 5 samples and (d) 40 samples, respectively.

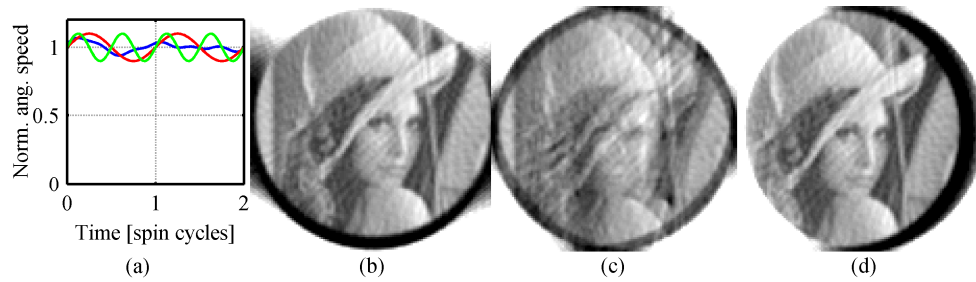


Fig. 12. (a) Rotational speeds variations with once (red curve) and twice (green) the rotational cycle frequency, and a general variation (blue). (b) Reconstruction with sinusoidal scan speed variations with a frequency corresponding to one spin cycle, creating a difference between nominal and actual sampling location varying between  $\pm 5$  samples. (c) Same as in (b), but with twice the scan speed variation frequency. (d) Reconstruction similar to that in Fig. 9(b), but with a horizontal reticle offset corresponding to 10% of the aperture diameter.

The reticle may be misaligned by sideways translation. The effect, shown in Fig. 12(d) with a misalignment representing 10% of the aperture diameter, resembles that in Fig. 12(b): A translated image with a border distortion image. Analytically, these cases are indeed similar.

To sum up, aperture alignment errors essentially produce FOV rim artefacts. Timing and reticle orientation offset is more serious, necessitating a precise angular measurement. It is desirable to avoid jitter in the speed of the scan rotation.

#### 5.6 Noise simulations for single- and multi-channel TOSCA configurations

The simulation includes photon noise and detector noise. Figure 13 shows simulation results for bright, medium and low light conditions. In bright light, reconstruction artefacts due to the finite number of angular scans represent the dominant distortion effect. Noise is a significant source of error at lower light levels. In Fig. 13(c) detector noise is the most significant deterioration. The pixel-level signal-to-noise ratio is here  $< 0.5$ , but the eye's spatial averaging capabilities still enables recognition of large features. For image sequences, temporal averaging could lower the feature recognition threshold even further.

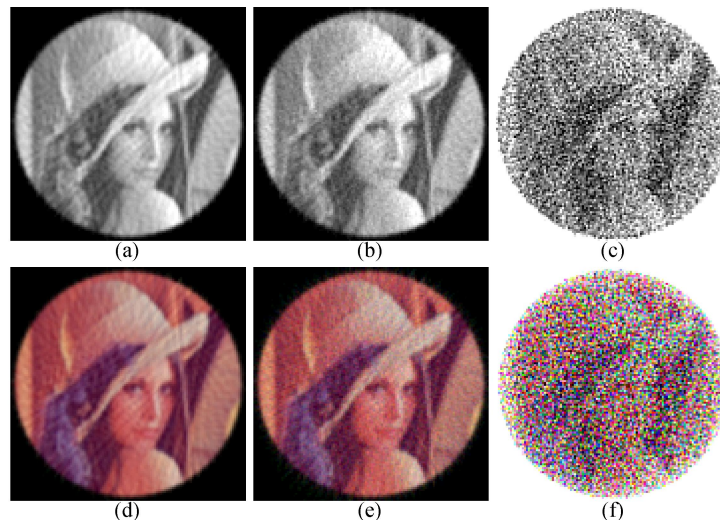


Fig. 13. Reconstruction with detector + photon noise in (a) bright, (b) medium, and (c) low light conditions, where the brightest pixel is scaled to have (a) the same spectral radiant exitance as the reference target in Fig. 7(a) ( $M_{l,max} = 350 \text{ Wm}^{-2}\mu\text{m}^{-1}$ ), (b)  $10^{-2}$  and (c)  $10^{-4}$  of the value in (a). (d)-(f): As in (a)-(c), but with the energy spread to 3 spectral channels.

In multi-channel systems, detectors share the signal photons. Photon noise is then also reduced, whereas the detector noise per channel remains the same. This is shown in Fig. 13(d), 13(e) and 13(f), where we have 3 channels in the same bright, medium and low light conditions as above. Noise is still not noticeable in the bright light image. In the medium light image, the noise is more significant than in the corresponding monochrome image, and the visual recognition threshold is approached in the low light image, with a signal-to-noise ratio less than 0.3.

## 6. Discussion

There are several ways to enhance the images, but enhancements often tend to be application specific. This is not the main topic of this paper, and only indications as to certain solutions will be given. Kak and Slaney give indications of several possibilities [3]. First, they indicate that the number of angular scans (or projections) should be roughly equal to the number of samples (or rays) per scan, but this is for a general image. Increasing the number of angular scans will reduce the relative ripple, but one then have to increase reticle scan radius, reduce the pixel size, or reduce the number of samples per scan. This is difficult due to design, mechanical and optomechanical constraints.

Adding intermediate scans using a linear interpolation of successive scans can typically remove artefacts in peripheral regions of the image, but at the same time introduce blur in the same locations. Instead of using the simple ramp filter described above, one might choose a modified back projection filter to remove frequency components that are known not to exist in the image, or remove or dampen undesirable components.

It is seen that Fig. 8(b) and 8(c) contains artefacts around the main lobe. These ripples are mainly due to the limited number of angles and the mismatch between a circular and rectangular grid. The first limitation is fundamental, but in the case of the latter, better approximations to the discrete Radon transform employed here could be used [12]. Improved inverse transforms could flatten the area close to the main lobe and narrow the main lobe.

One could also calculate the point spread function of the image, and determine some kind of inverse function to reduce artefacts through convolution. Unfortunately, the point spread function is position dependent, as shown in Fig. 4(b) and 4(c), rendering this task difficult.

It is also possible to use iterative approaches, where the reconstructed image is sent through a construction process. Ideally, this would recreate the original signal, but the difference obtained can be used to modify the reconstruction. This process can be repeated until the error is sufficiently small, provided the process converges. This process is susceptible to noise. An inconvenience is that the iterative process can be time consuming, and will typically not be interesting in real-time applications. In images with high contrast, particularly in the presence of a few very bright “hot spots”, signals corresponding to images of these bright objects could be generated and subtracted from the original signal. This simplified iterative approach could potentially remove the biggest artefacts, easing the image analysis.

High frequency illumination variations, low light conditions and strongly asymmetric scene illumination is likely to affect system performance, calling for a more direct scan speed control, but the current solution was deemed sufficient for the demonstration. An optical encoding pattern outside the thin slit reticle pattern could be used as an angular reference.

Better roller bearings and fixtures would be costlier, but could reduce mechanical vibrations and lead to a smaller spot size, enabling a smaller reticle or higher resolution.

The focusing/collimating optics could be separated from the rotating unit, enabling better and more flexible optics. In the setup, focus was adjusted by optics in front of the system.

## 7. Conclusion

This paper presents the first working tomographic scanning (TOSCA) imager. Detailed analysis first show that an imaging camera system using a single pixel sensor and a simple circular scan mechanism can operate as a photon noise limited system in realistic lightning conditions with existing optical and electro-optical components. A detailed physics-based

simulation was used to quantify the effect of error sources such as misalignment, temporal sampling errors and scan speed variations. The analysis identified the need for a precise angular reference, but initial simulations indicated that it might not be necessary to have detailed angular position readout for each sample, provided rotational inertia is significant. The effect of noise was also examined through simulation, supporting the initial assumption that the system should have adequate performance. The proposed configuration has some limitations in pure imaging due to a low number of angular scan orientations creating characteristic line artefacts, but is sufficient if objects of interest are located on an otherwise homogeneous background, as artefacts manifests themselves at a distance from the object of interest. Measurements using the experimental setup verified the performance predicted through theory and simulations. Advantages of the inherent geometric co-registration of several spectral channels were highlighted and demonstrated.

### **Acknowledgments**

The author is grateful to Prof. Svein Erik Hamran and Dr. Torbjørn Skauli for helpful discussions and able guidance, to Dr. Stéphane Nicolas for doing the ZEMAX simulations, and to Mr. Sverre Dyrkorn for doing the SolidWorks construction of the camera.